Available online at http://scik.org
Commun. Math. Biol. Neurosci. 2025, 2025:27
https://doi.org/10.28919/cmbn/9105
ISSN: 2052-2541

SENSITIVITY PARAMETER FOR A DISCRETE-TIME LOGISTIC MELANOMA CELL GROWTH UNDER VIROTHERAPY

VISKA NOVIANTRI[1,*], FELICIA AURELIA SUWANDI[1,2]

[1]Mathematics Department, School of Computer Science, Binus University, Jakarta, 11480, Indonesia

[2]Computer Science Department, School of Computer Science, Binus University, Jakarta, 11480, Indonesia

Abstract. Melanoma is a rare type of skin cancer but the most serious compared to other types of skin cancer. The study of melanoma growth is interesting to analyze so that related parties can determine how quickly this cancer spreads and determine the proper and efficient treatment method. This paper uses the mathematical modeling of tumor growth to describe melanoma growth in the presence of virotherapy. The model shows the interaction between melanoma and uninfected tumor cells, completed by a Logistic law as a classical fraction for population growth to represent the natural melanoma growth function. Then, this model is discretized by the Non-Standard Finite Difference Method, then solved numerically, and completed by the 4th Runge Kutta method for validation. Moreover, this study gave a sensitivity analysis of several parameters to see how much melanoma growth changes over these parameters. Finally, it can be shown that the melanoma cell growth rate and virotherapy rate have the most significant effect on the number of melanoma cells.

Keywords: tumor dynamical system; logistic growth; non-standard finite difference method; sensitivity analysis.

2020 AMS Subject Classification: 34A34, 34B60, 65L05.

1. INTRODUCTION

Skin tumors are the most common skin findings and become reasons for consulting a dermatologist [1], [2]. Like other tumors, skin tumors can be benign (non-cancerous) and malignant

*Corresponding author

E-mail address: viskanoviantri@binus.ac.id

Received January 04, 2024

(cancerous). Skin cancer is an abnormal growth of skin cells, usually caused by ultraviolet (UV) radiation overexposure. This cancer can become a global threat to health and is expected to increase rapidly in the next 20 years if not diagnosed at an early stage [3]. There are three types of skin cancer: basal cell carcinoma, squamous cell carcinoma, and melanoma. These first two types are the most common and known as non-melanoma skin cancer, whereas melanoma is rare but the most aggressive and deadliest skin cancer[4], [5], [6], [7]. In 2020, Arnold et al. [8] stated from global cancer data that there were 325000 new melanoma cases and 57000 deaths due to melanoma. If 2020 rates continue, they expect the burden of melanoma is likely to increase by 50% for new cases and increase in deaths by 68% by 2040.

Melanoma early detection becomes an essential thing for better outcomes so that the mortality because of it can be reduced [9]. Some technological innovations, including novel communication and imaging tools, are developed to help dermatology in melanoma diagnosis [10]. A systematic review of eligible publications in periods 2018 - 2022 shows that perform of several Artificial Intelligence (AI) techniques as well as or better than dermatologists in detecting melanoma [11]. A comprehensive survey also shows that the machine/deep learning approach can help skin lesion analysis detect melanoma [12]. Furthermore, there are at-home testing can be applied to detect melanoma without the help of a skin specialist [13].

It is also important to carry out studies on predicting melanoma growth both with or without the treatment. By this prediction, optimizing the treatment efficacy can be derived. Melanoma growth in medical and biological science can be derived by in vivo and in vitro experiments such as the xenograft model in blood serum and tissue [14], growth hormone receptor [15]. Deep learning methods can help these experiments to get more information in forecasting and predicting melanoma growth [16], [17], [18], [19]. Furthermore, many mathematicians use mathematical models to describe tumor and cancer growth dynamics, including melanoma.

This study applied two nonlinear differential equations models that represent uninfected and infected (melanoma) cell populations in tumor cells based on some biological parameters. The model conducts the competition between the infected and uninfected cells in tumor cells as predator and prey. In the previous research [20], the gompertzian model use to describe the cell population growth. In this research, the logistic growth function is chosen here to describe

classical biology for tumor cell population growth. This model is completed by a virotherapy parameter as a melanoma treatment. Then, the Non-Standard Finite Difference (NSFD) scheme constructed the discrete-time model version and compared it to the 4^{th} Runge Kutta scheme for validity. The numerical solution and simulations are completed by sensitivity analysis to investigate the model response when one parameter is varied, and other parameters are held as constants. The results show that the infected (melanoma) cell population is the most affected by the virotherapy parameter. In contrast, the uninfected cell population is the most affected by the immune system parameter.

2. Dynamical System of Logistic Melanoma Cell

The population of tumor cells divides into uninfected non-cancerous cells and infected cancer cells, which mutually influence each other [21]. Interaction between uninfected cells and infected cells can be described by a modified Lotka-Volterra model where infected cells are the predators of uninfected cells. Next, the infected cell is named a melanoma cell since this paper discusses the dynamical system of melanoma cell growth. Let $x(t)$ and $y(t)$ be the number of uninfected cells and melanoma cells over time t so that a nonlinear system describes their dynamical interaction:

$$\frac{dx}{dt} = uxG(x,y) - \delta x - \beta xy, \tag{1}$$

$$\frac{dy}{dt} = \beta xy + myG(x,y) - \alpha y, \tag{2}$$

where the terms $uxG(x,y)$ in (1) and $myG(x,y)$ in (2) describe increasing number of uninfected and melanoma cells because of biological models' classical fractional population growth $G(x,y)$, respectively. Here, u is the uninfected growth rate and m is the melanoma cell growth rate, which will enhance in each population number. The transmission rate between uninfected and melanoma cells is interpreted by β. It can reduce the number of uninfected cells but increases the number of melanoma cells. The number of uninfected cells may decrease because of the immune system by rate δ. The presence of virotherapy can reduce the number of melanoma cells by rate α. In this study, the function $G(x,y)$ represents a logistic model so that:

$$G(x,y) = 1 - \frac{x+y}{k}, \tag{3}$$

where k is carrying capacity.

3. STABILITY CRITERIA

TABLE 1. Equilibrium points and their stability criteria

Equilibrium Point	Eigen Value	Stability Criteria
E_1	$\lambda_1 = u - \delta$	$u < \delta$
	$\lambda_2 = -\alpha + m$	$m < \alpha$
E_2	$\lambda_1 = \frac{\alpha}{m}(u + \beta k) - \delta - \beta k$	$\alpha < \frac{m(\delta+\beta k)}{u\beta k}$
	$\lambda_2 = \alpha - m$	$\alpha < m$
E_3	$\lambda_1 = -u + \delta$	$u > \delta$
	$\lambda_2 = \frac{\delta}{u}(m - \beta k) - \alpha + \beta k - \delta$	$\alpha > \frac{\delta}{u}(m - \beta k) - \delta$
E_4	$\lambda_{1,2} = \frac{-A \pm \sqrt{A^2 - 4B}}{2}$	$B > 0$
	$A = -A_1 - A_2$	
	$B = A_1 A_2$	
	$A_1 = m\left(1 - \frac{x^* + 2y^*}{k}\right) - \alpha + \beta x^*$	
	$A_2 = u\left(1 - \frac{2x^* + y^*}{k}\right) - \delta - \beta y^*$	

Stability criteria for the logistic model (1) - (3) can be derived starting from its equilibrium point. Using the logistic function (3) and setting the dynamical system (1) - (2) equal to zero, then four equilibrium points obtained as follows:

$$E_1 = (0,0); E_2 = \left(0, \frac{k(m-\alpha)}{m})\right); E_3 = \left(\frac{k(u-\delta)}{u}, 0\right), \tag{4}$$

$$E_4 = (x^*, y^*) = \left(\frac{-\alpha u + \delta m + \beta k m - \alpha\beta k}{-\beta u - k\beta^2 + \beta m}, k - \frac{k(\alpha - \beta x^*)}{m} - x^*\right), \tag{5}$$

where E_1 indicates that no tumor cells are found in the body. In contrast, E_2 and E_3 show the presence of tumor cells. Furthermore, E_2 shows that all tumor cells are melanoma cells but E_3 indicates that all tumor cells are uninfected. In E_4, some tumor cell becomes melanoma cell and the others are still as uninfected cells.

Next, the stability of each equilibrium point can be derived by solving the characteristic equation $det(\lambda I - J) = 0$ for λ, where J is the Jacobian matrix for a nonlinear system (1) and (2):

$$J = \begin{pmatrix} u\left(1 - \frac{2x+y}{k}\right) - \delta - \beta y & -\left(\frac{u}{k} + \beta\right) x \\ -\left(\frac{m}{k} - \beta\right) y & m\left(1 - \frac{x+2y}{k}\right) - \alpha + \beta x \end{pmatrix}. \tag{6}$$

Substitute each equilibrium point in (4) and (5) into (6), then the characteristic equation will give the eigenvalue for each equilibrium point. The equilibrium point is stable if and only if a real part of each eigenvalue is negative. The stability criteria for each equilibrium point are shown in Table 1.

4. Discrete Time Model of Logistic Melanoma Cell Growth

The discrete-time form for the nonlinear dynamical system (1) – (2) will solved numerically by the Non-Standard Finite Difference (NSFD) method. Let the differential equation system.

$$\frac{d\varepsilon}{dt} = F(\varepsilon, \omega), \tag{7}$$

where $\varepsilon = x, y$, ω is a parameter set, and $F(\varepsilon, \omega)$ is a continuous nonlinear function with a continuous partial derivative in the domain. According to Mickens [???], the NSFD scheme related to the nonlinear system (7) is

$$\frac{\varepsilon_{n+1} - \Psi \varepsilon_n}{\Phi} = F(\varepsilon_n, \omega), \tag{8}$$

where Ψ and Φ are functions depending on the eigenvalues (λ_1, λ_2) which are obtained by section 2, and time step size $\Delta t = t_{n+1} - t_n$, as follows

$$\Psi(\lambda_1, \lambda_2, \Delta t) = \frac{\lambda_1 e^{\lambda_2 \Delta t} - \lambda_2 e^{\lambda_1 \Delta t}}{\lambda_1 - \lambda_2}, \tag{9}$$

$$\Phi(\lambda_1, \lambda_2, \Delta t) = \frac{e^{\lambda_1 \Delta t} - e^{\lambda_2 \Delta t}}{\lambda_1 - \lambda_2}. \tag{10}$$

Furthermore, the eigenvalues for equilibrium point E_4 may be complex numbers. Let $\lambda_{1,2} = a \pm bi$ where a and b a real and imaginary parts of the eigenvalue, respectively, then equations

(9) and (10) become

$$\Psi(\lambda_1,\lambda_2,\Delta t) = \frac{1}{b}e^{a\Delta t}(b\cos(b\Delta t) - a\sin(b\Delta t)) \tag{11}$$

$$\Phi(\lambda_1,\lambda_2,\Delta t) = \frac{1}{b}e^{a\Delta t}\sin(b\Delta t). \tag{12}$$

Apply (8) into (1) and (2), so that the NSFD scheme for this nonlinear model becomes,

$$\frac{x_{n+1}-\Psi x_n}{\Phi} = ux_n\left(1-\frac{x_n+y_n}{k}\right) - \delta x_n - \beta x_n y_n, \tag{13}$$

$$\frac{y_{n+1}-\Psi y_n}{\Phi} = \beta x_n y_n + my_n\left(1-\frac{x_n+y_n}{k}\right) - \alpha y_n, \tag{14}$$

where x_0 and y_0 are initial condition with $n = 1,2,...$

5. Results and Analysis

5.1. Numerical Simulation. Four simulations were conducted to see the tumor cell growth behavior related to each equilibrium point based on input parameters as in Table 2. In this table, δ is assumed, while the other parameter values are derived from previous research [22]. By checking and calculating the parameter input in Table 2 for the stability criteria in Table 1, it can be derived that each simulation leads to a different equilibrium point with their eigenvalues as in Table 3. Simulation 1-3 has a negative real eigenvalue while Simulation 4 gives a complex eigenvalue with a negative real part.

Tumor cell number over time generated by NSFD scheme (13) – (14), using (9) – (10) for Simulation 1 - 3 and (11) – (12) for Simulation 4 since its eigenvalue is a complex number. These numerical simulations also validate with the 4th Runge Kutta scheme by calculating the difference value using the following formula:

$$\Delta\varepsilon_n = |\varepsilon_n(NSFD) - \varepsilon_n(RK)| \tag{15}$$

where $\Delta\varepsilon_n = \Delta x_n, \Delta y_n$ describe the cell number difference between NSFD value $\varepsilon_n(NSFD)$ and Runge Kutta $\varepsilon_n(RK)$. The results for Simulation 1 – 4 are shown in Figure 1 – 4, respectively. Each figure consists of four sub-figures: (a) Cell number over time by NSFD scheme, (b) Cell number over time by 4th Runge Kutta scheme, (c) Cell number differences between NSFD and Runge Kutta based on formula (15), and (d) Phase portrait.

TABLE 2. Parameter Data

Simulation	u	m	δ	β	α	k	h	x_0	y_0	T
1^{st}	0.1	0.2000	0.2	1.4000	0.2500	1	0.01	0.1	0.35	150
2^{nd}	1	0.5311	0.2	1.4000	0.3000	1	0.01	0.1	0.35	150
3^{rd}	1	0.5311	0.2	0.2529	1.2936	1	0.01	0.1	0.35	150
4^{th}	1	0.5311	0.2	2.5291	1.2936	1	0.01	0.1	0.35	150

TABLE 3. Equilibrium Points and Their Eigenvalues

Simulation	Equilibrium Point	Eigenvalue
1^{st}	$E_1 = (0,0)$	$\lambda_1 = -0.0499, \lambda_2 = -0.1$
2^{nd}	$E_2 = (0;0.4351)$	$\lambda_1 = -0.2311, \lambda_2 = -0.2443$
3^{rd}	$E_3 = (0.8;0)$	$\lambda_1 = -0.7999, \lambda_2 = -0.9851$
4^{th}	$E_4 = (0.4109, 0.1102)$	$\lambda_{1,2} = -0.2347 \pm 0.5920i$

In Simulation 1, Figures 1 (a) and (b) show that the number of uninfected and infected cells have the same pattern even though different numerical schemes approximate them. Uninfected and infected cell numbers decrease before reaching their equilibrium point $E_1(0,0)$. The uninfected cell goes to equilibrium point $E_1(0,0)$ faster than infected cells since the initial value of the uninfected cell is closer to E_1 than the infected cell. Quantitatively, the NSFD and Runge Kutta results are almost the same since the maximum difference between them is only 8×10^{-5} as in Figure 1(c). The difference value for infected (Δx) and uninfected cells (Δy) reach the maximum value at time $t \approx 3$. The difference value of the infected cell (Δy) fluctuates more than the infected cell (Δy), but they converge to 0. The phase portrait for Simulation 1 shows that E_1 is asymptotic stable as in Figure 1 (d), which is appropriate with its negative eigenvalues. The trajectory starts from (x_0, y_0)=(0.35,0.1) then goes to $E_1 = (0,0)$ as time increase. In this case, E_1 describes that virotherapy is successful in killing all tumor cells.

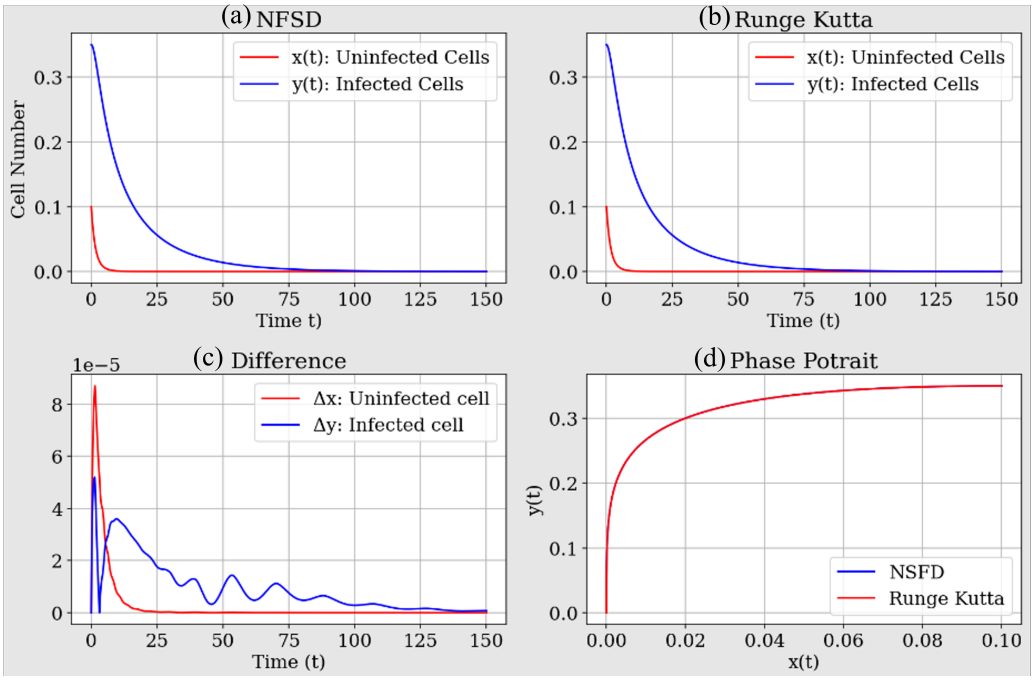

FIGURE 1. Simulation 1 results

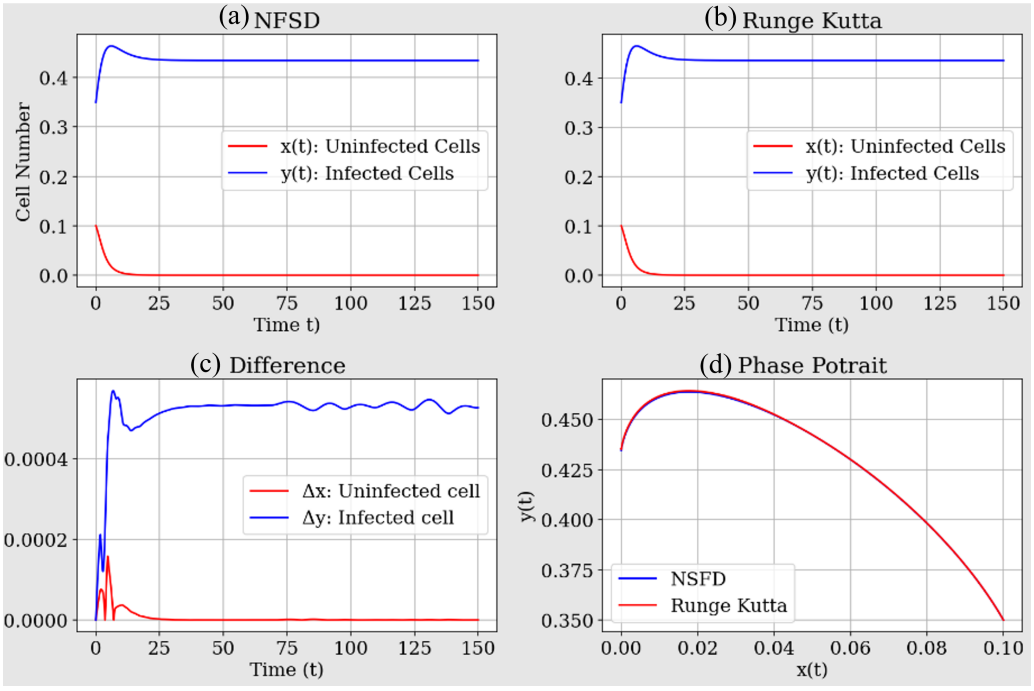

FIGURE 2. Simulation 2 results

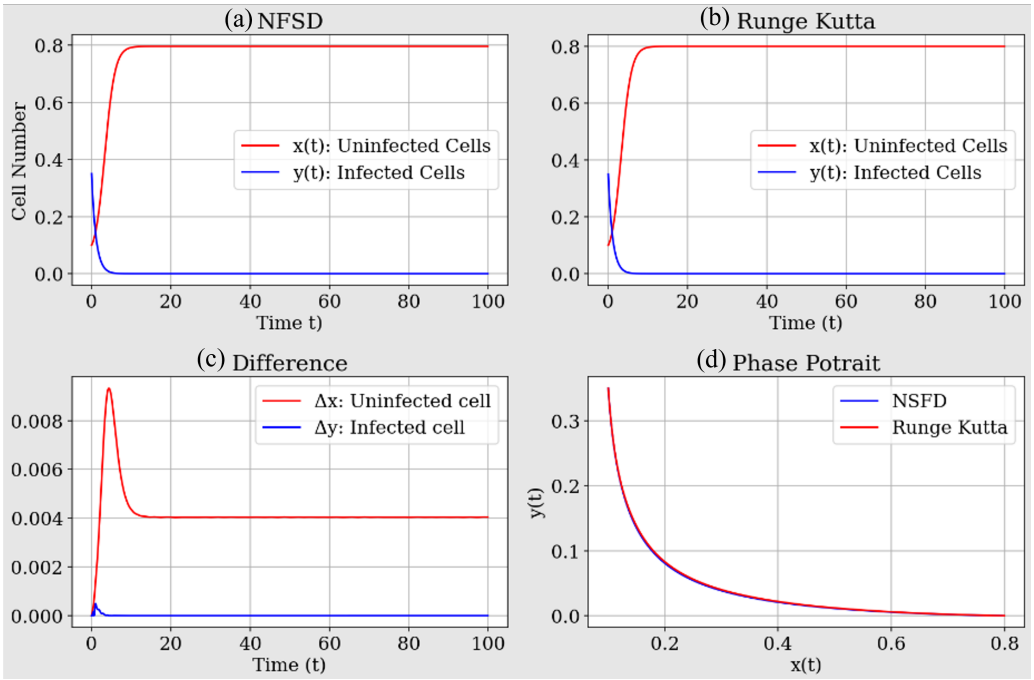

FIGURE 3. Simulation 3 results

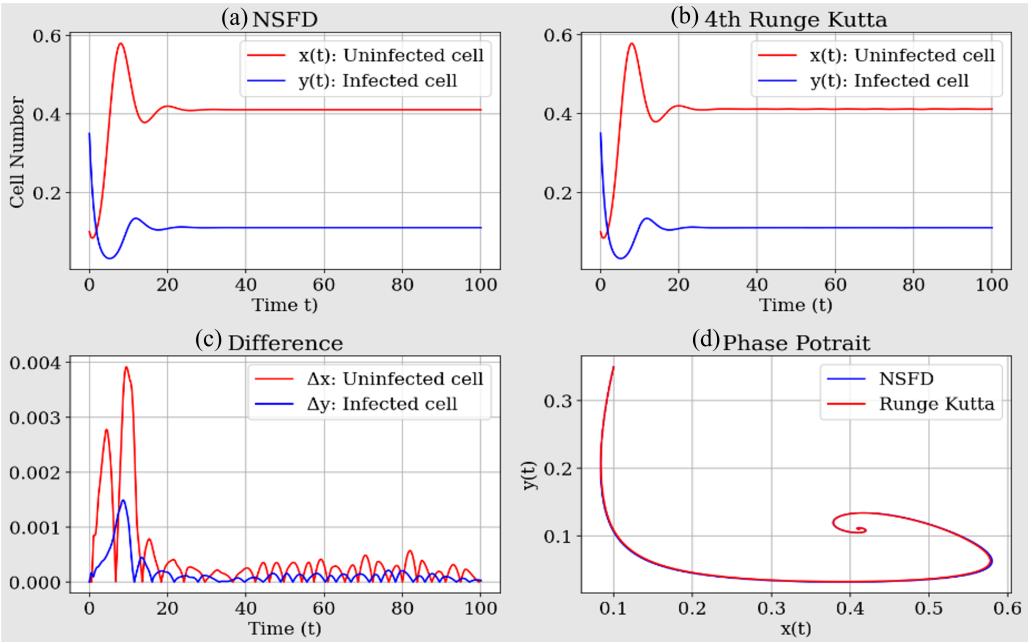

FIGURE 4. Simulation 4 results

The same qualitative results between NSFD and Runge Kutta occur in Simulation 2, as in Figures 2 (a) and (b). Both sub-figures show that the uninfected and infected cell numbers grow in the opposite direction, even though the infected cell slightly fluctuates at time $t < 25$. When $t > 25$, the infected cell numbers will stable at 0.4351, while the uninfected cell numbers decrease and become 0 at $t < 12$. These numerical results are appropriate with the analytical results that Simulation 2 will converge to $E_2 = (0, 0.4351)$. This condition tells us that all tumor cells found in the body become infected. The difference Δx over time is always smaller than Δy as in Figure 2(c). The maximum Δx and Δy reach at time $t \approx 5$ with values less than ≈ 0.0002 and 0.0006, respectively. Next, the trajectory for this simulation starts from $(x_0, y_0) = (0.1, 0.35)$ then goes to E_2 shown in Figure 2(d).

The numerical results for Simulation 3 are given in Figure 3. The NSFD (a) and Runge Kutta (b) results describe that the uninfected and infected cells grow in the opposite direction for very short periods before going constant. Here, the infected cell numbers drop quickly to 0 and the uninfected cell numbers grow to 0.8, then stable afterward. It is aligned with the analytical solution in Table 3 that Simulation 3 will stable to equilibrium point $E_3 = (0.8, 0)$. The difference between NSFD and Runge Kutta for tumor cell numbers is plotted in subfigure (c). Based on Figures 2(c) and 3(c), Simulation 2 and 3 give Δx and Δy in the opposite behavior. In Figure 3(c), Δx is always greater than Δy. The maximum difference for Δx and Δy in Simulation 3 are less than 0.009 and less than 0.001, respectively. As in subfigure 1(d) and 2(d), subfigure 3(d) has a similar phase portrait, which is the equilibrium point type is a node and asymptotic stable since $\lambda_2 < \lambda_1 < 0$.

Figure 4 shows the numerical results for Simulation 4. Similar to sub-figures 1(a)-(b), 2(a)-(b), and 3(a)-(b), sub-figure 4(a)-(b) gives the same qualitative results between NSFD and Runge Kutta to approximate the number of uninfected and infected cells. Unlike previous simulations, Simulation 4 shows that the number of uninfected and infected cells fluctuates more before reaching equilibrium. Moreover, when $t > 2$, uninfected cells are always greater than infected cells. Both sub-figures show that the uninfected and infected cells converge, which describes the condition where the tumor consists of uninfected and infected cells. The fluctuating results also show in the difference value Δx and Δy as in Figure 4(c), with the maximum

difference for Δx and Δy is less than 0.004 and 0.002, respectively. Nevertheless, the difference Δx and Δy is asymptotic stable and follows the uninfected and infected cells pattern over time. These results align with the phase portrait as in sub-figure 4(d). This sub-figure shows that the trajectory starts from (x_0, y_0) and then goes to E_4 as a spiral point since the eigenvalues for E_4 are complex numbers with negative real parts.

Based on Simulation 1-4 results, it can be concluded that the numerical results of all simulations follow the analytical results in Table 2. The NSFD scheme has a small difference from the 4th Runge Kutta scheme so the NSFD scheme successfully approximates the number of uninfected and infected cells. Furthermore, Simulation 1- 4 has the same results as the other research [23].

5.2. Sensitivity Analysis. The sensitivity analysis applied here investigates the model response when one parameter is varied and holds other parameters as a constant. For the differential equation system (7), the parameter sensitivity can be described through the following differential equation system:

$$\frac{d}{dt}\left(\frac{\partial \varepsilon}{\partial \omega}\right) = J\frac{\partial \varepsilon}{\partial \omega} + \frac{\partial F}{\partial \omega} \tag{16}$$

where J is a 2×2 Jacobian matrix (6).

Interesting parameters to investigate the model response (1) and (2) are $u, m, \delta, \beta, \alpha$ so that $\frac{\partial \varepsilon}{\partial \omega}$ and $\frac{\partial F}{\partial \omega}$ are 2×5 matrix as follows:

$$\frac{\partial \varepsilon}{\partial \omega} = \begin{pmatrix} \frac{\partial x}{\partial u} & \frac{\partial x}{\partial m} & \frac{\partial x}{\partial \delta} & \frac{\partial x}{\partial \beta} & \frac{\partial x}{\partial \alpha} \\ \frac{\partial y}{\partial u} & \frac{\partial y}{\partial m} & \frac{\partial y}{\partial \delta} & \frac{\partial y}{\partial \beta} & \frac{\partial y}{\partial \alpha} \end{pmatrix}, \tag{17}$$

$$\frac{\partial F}{\partial \omega} = \begin{pmatrix} x\left(1-\frac{x+y}{k}\right) & 0 & -x & -xy & 0 \\ 0 & y\left(1-\frac{x+y}{k}\right) & 0 & xy & -y \end{pmatrix}. \tag{18}$$

Next, the differential equation system (16) is solved numerically by the 4th Runge Kutta scheme based on parameter data in Tables 2 and 3. These numerical simulations represent parameter sensitivity in different equilibrium points. Figure 5 - 8 show the sensitivity parameter for equilibrium point E_1 (Simulation 1), E_2 (Simulation 2), E_3 (Simulation 1), and E_4 (Simulation 4), respectively. These figures are organized into two columns, where each column visually

represents the sensitivity level of the parameters investigated for the uninfected and infected cell population. From all simulations, only Simulations 4 in Figure 8 show that the sensitivity levels for each parameter are asymptotic stable. Since all parameters fluctuate quickly at time $t < 30$, it is difficult to investigate the most significant parameter of the cell population alterations in Simulation 4. However, the impact of all parameters can be seen clearly when time $t > 30$, since all are stable. It can be seen that parameter α becomes the most significant impact on the cell alterations. This implies that higher virotherapy can reduce the number of melanoma cells and increase uninfected cells significantly. In contrast, an uninfected growth rate leads to increasing melanoma cells.

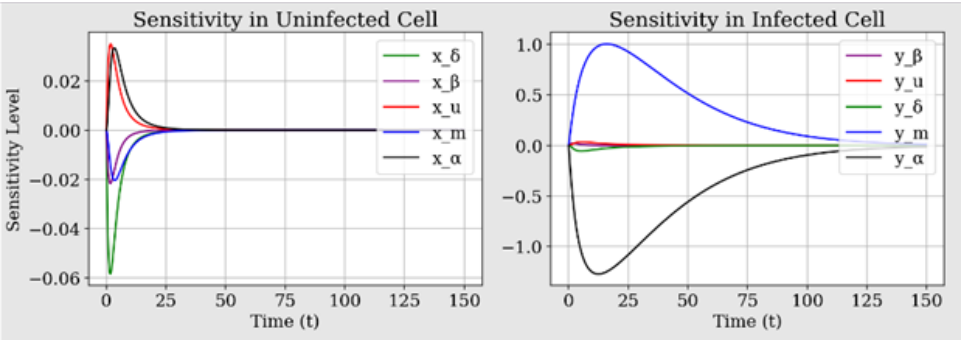

FIGURE 5. Sensitivity Parameter for Simulation 1

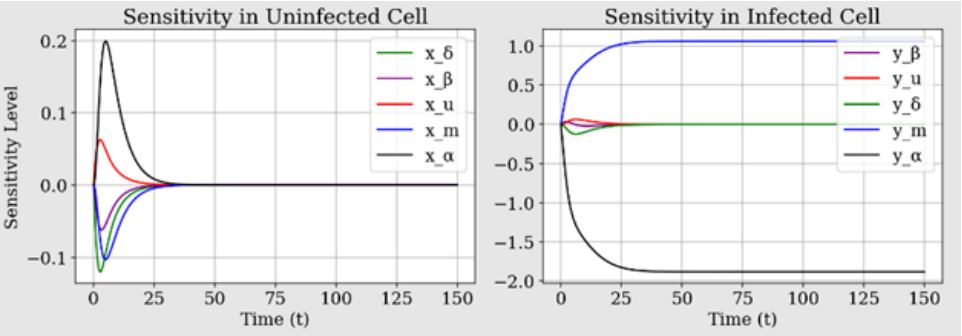

FIGURE 6. Sensitivity Parameter for Simulation 2

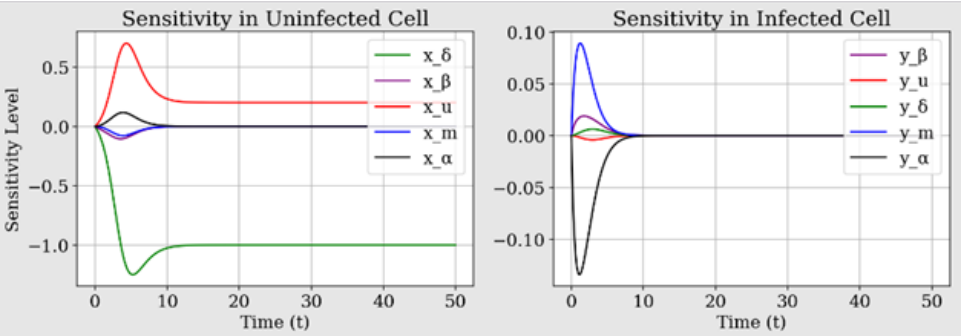

FIGURE 7. Sensitivity Parameter for Simulation 3

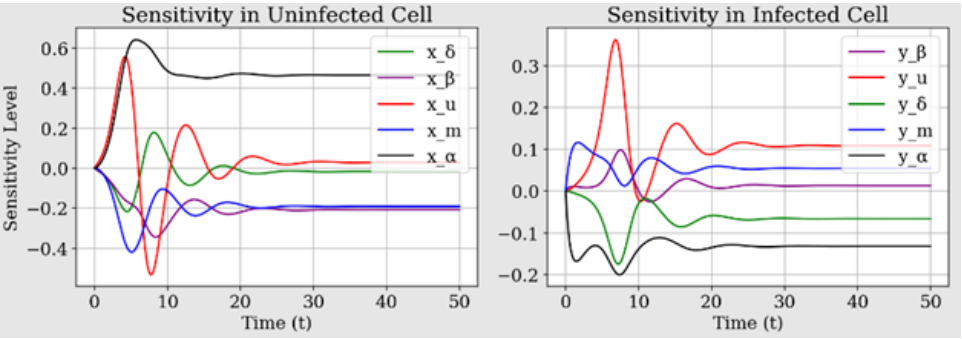

FIGURE 8. Sensitivity Parameter for Simulation 4

In Simulations 1-3, parameters α and m have the most significant impact on the melanoma cell alterations. As in Simulation 4, the virotherapy rate (α) can reduce the melanoma cell population significantly, in contrast with the melanoma cell growth rate (m). Furthermore, the immune system (δ) is the most parameter that can reduce the uninfected cell. However, the impact of each parameter on the uninfected cell is slightly different.

6. CONCLUSION

The logistic growth function has successfully modelled the mathematical interaction between uninfected cells and melanoma cells under virotherapy treatment. Explicitly, this model generates four equilibrium points representing free tumor cells, free uninfected cells, free melanoma cells, and the presence of uninfected and melanoma cells (interior equilibrium). All equilibrium points are conditionally stable, where their eigenvalues can be used to derive the numerical scheme, Non-Standard Finite Difference (NSFD) method. This numerical scheme has a high

accuracy since the difference is less than 0.9% compared to the 4th Runge Kutta Scheme. The simulation results show that the uninfected and melanoma grow in different directions for all equilibrium points, except in interior equilibrium. Furthermore, the sensitivity analysis shows that higher virotherapy can reduce the number of melanoma cells and increase uninfected cells significantly.

CREDIT AUTHORSHIP CONTRIBUTION STATEMENT

Viska Noviantri: Writing – original draft, review, and editing, Methodology, Investigation, Formal analysis, Conceptualization, Validation. Felicia Aurelia Suwandi: Algorithm implementation, Software, Visualization.

CONFLICT OF INTERESTS

The authors declare that there is no conflict of interests.

REFERENCES

[1] V. Gruber, R. Hofmann-Wellenhof, P. Wolf, et al. Common Benign Melanocytic and Non-Melanocytic Skin Tumors among the Elderly: Results of the Graz Study on Health and Aging, Dermatology 239 (2023), 379–386. https://doi.org/10.1159/000529219.

[2] J. Huang, L. Zhang, L. Shi, et al. An Epidemiological Study on Skin Tumors of the Elderly in a Community in Shanghai, China, Sci. Rep. 13 (2023), 4441. https://doi.org/10.1038/s41598-023-29012-1.

[3] N. Hasan, A. Nadaf, M. Imran, et al. Skin Cancer: Understanding the Journey of Transformation from Conventional to Advanced Treatment Approaches, Mol. Cancer 22 (2023), 168. https://doi.org/10.1186/s12943-023-01854-3.

[4] C. Garrubba, K. Donkers, Skin Cancer, J. Am. Acad. Physician Assist. 33 (2020), 49–50. https://doi.org/10.1097/01.JAA.0000651756.15106.3e.

[5] M. Cives, F. Mannavola, L. Lospalluti, et al. Non-Melanoma Skin Cancers: Biological and Clinical Features, Int. J. Mol. Sci. 21 (2020), 5394. https://doi.org/10.3390/ijms21155394.

[6] J. Chandra, N. Hasan, N. Nasir, et al. Nanotechnology-Empowered Strategies in Treatment of Skin Cancer, Environ. Res. 235 (2023), 116649. https://doi.org/10.1016/j.envres.2023.116649.

[7] R. Tow, S. Hanoun, B. Andresen, et al. Recent Advances in Clinical Research for Skin Cancer Chemoprevention, Cancers 15 (2023), 3819. https://doi.org/10.3390/cancers15153819.

[8] M. Arnold, D. Singh, M. Laversanne, et al. Global Burden of Cutaneous Melanoma in 2020 and Projections to 2040, JAMA Dermatol. 158 (2022), 495. https://doi.org/10.1001/jamadermatol.2022.0160.

[9] M.J. Diaz, I. Mark, D. Rodriguez, et al. Melanoma Brain Metastases: A Systematic Review of Opportunities for Earlier Detection, Diagnosis, and Treatment, Life 13 (2023), 828. https://doi.org/10.3390/life13030828.

[10] T. Petrie, R. Samatham, A.M. Witkowski, A. Esteva, S.A. Leachman, Melanoma Early Detection: Big Data, Bigger Picture, J. Invest. Dermatol. 139 (2019), 25–30. https://doi.org/10.1016/j.jid.2018.06.187.

[11] R.H. Patel, E.A. Foltz, A. Witkowski, J. Ludzik, Analysis of Artificial Intelligence-Based Approaches Applied to Non-Invasive Imaging for Early Detection of Melanoma: A Systematic Review, Cancers 15 (2023), 4694. https://doi.org/10.3390/cancers15194694.

[12] M. Zafar, M.I. Sharif, M.I. Sharif, et al. Skin Lesion Analysis and Cancer Detection Based on Machine/Deep Learning Techniques: A Comprehensive Survey, Life 13 (2023), 146. https://doi.org/10.3390/life13010146.

[13] Z.R. Garrison, C.M. Hall, R.M. Fey, et al. Advances in Early Detection of Melanoma and the Future of At-Home Testing, Life 13 (2023), 974. https://doi.org/10.3390/life13040974.

[14] M. Adhikari, B. Adhikari, N. Kaushik, et al. Melanoma Growth Analysis in Blood Serum and Tissue Using Xenograft Model with Response to Cold Atmospheric Plasma Activated Medium, Appl. Sci. 9 (2019), 4227. https://doi.org/10.3390/app9204227.

[15] R. Basu, S. Wu, J.J. Kopchick, Targeting Growth Hormone Receptor in Human Melanoma Cells Attenuates Tumor Progression and Epithelial Mesenchymal Transition via Suppression of Multiple Oncogenic Pathways, Oncotarget 8 (2017), 21579–21598. https://doi.org/10.18632/oncotarget.15375.

[16] A. Zaritsky, A.R. Jamieson, E.S. Welf, A. Nevarez, et al. Interpretable Deep Learning Uncovers Cellular Properties in Label-Free Live Cell Images That Are Predictive of Highly Metastatic Melanoma, Cell Syst. 12 (2021), 733-747.e6. https://doi.org/10.1016/j.cels.2021.05.003.

[17] H. Du, Y. He, W. Lu, Y. Han, Q. Wan, Machine Learning Analysis of Immune Cells for Diagnosis and Prognosis of Cutaneous Melanoma, J. Oncol. 2022 (2022), 7357637. https://doi.org/10.1155/2022/7357637.

[18] J. Couetil, Z. Liu, K. Huang, J. Zhang, A.K. Alomari, Predicting Melanoma Survival and Metastasis with Interpretable Histopathological Features and Machine Learning Models, Front. Med. 9 (2023), 1029227. https://doi.org/10.3389/fmed.2022.1029227.

[19] R. Ashtagi, D. Mane, M. Deore, J.R. Maranur, S. Hosmani, Combined Deep Learning and Machine Learning Models for the Prediction of Stages of Melanoma, J. Auton. Intell. 7 (2023), 1–13. https://doi.org/10.32629/jai.v7i1.749.

[20] V. Noviantri, F.A. Suwandi, Gompertzian Tumor Cell Growth Using a Discrete Dynamic Model, Procedia Computer Sci. 245 (2024), 49–56. https://doi.org/10.1016/j.procs.2024.10.228.

[21] P.W. Ewald, H.A. Swain Ewald, The Scope of Viral Causation of Human Cancers: Interpreting Virus Density from an Evolutionary Perspective, Philos. Trans. R. Soc. B Biol. Sci. 374 (2019), 20180304. https://doi.org/10.1098/rstb.2018.0304.

[22] T. Ramaj, X. Zou, On the Treatment of Melanoma: A Mathematical Model of Oncolytic Virotherapy, Math. Biosci. 365 (2023), 109073. https://doi.org/10.1016/j.mbs.2023.109073.

[23] S. Udomchalermpat, S. Koonpraseart, E. Kunnawuttipreechachan, Dynamics of the Generalized Tumor-Virotherapy Model with Time Delay Effect, Eng. Lett. 28 (2020), 1–11.